IOPscience iopscience.iop.org

Home Search Collections Journals About Contact us My IOPscience

Unsteady immiscible multiphase flow validation of a multiple-relaxation-time lattice Boltzmann method

This content has been downloaded from IOPscience. Please scroll down to see the full text.

2014 J. Phys. A: Math. Theor. 47 105501

(http://iopscience.iop.org/1751-8121/47/10/105501)

View the table of contents for this issue, or go to the journal homepage for more

Download details:

IP Address: 138.250.179.90
This content was downloaded on 11/06/2017 at 12:57

Please note that terms and conditions apply.

You may also be interested in:

LBM for immiscible two-phase flows
T Reis and T N Phillips

Thermodynamic-consistent lattice Boltzmann model for nonideal fluids
Binghai Wen, Zhangrong Qin, Chaoying Zhang et al.

Hybrid multiple-relaxation-time lattice-Boltzmann finite-difference method for axisymmetric multiphase flows
Jun-Jie Huang, Haibo Huang, Chang Shu et al.

Multi-relaxation-time lattice Boltzmann front tracking method for two-phase flow with surface tension
Xie Hai-Qiong, Zeng Zhong, Zhang Liang-Qi et al.

Non-orthogonal central moments relaxing to a discrete equilibrium: A D2Q9 lattice Boltzmann model
Alessandro De Rosis

FFT-LB Modeling of Thermal Liquid-Vapor System
Gan Yan-Biao, Xu Ai-Guo, Zhang Guang-Cai et al.

Multiple-relaxation-time lattice Boltzmann approach to compressible flows with flexible specific-heat ratio and Prandtl number
Feng Chen, Aiguo Xu, Guangcai Zhang et al.

Moment equations for magnetohydrodynamics
P J Dellar

IOP Publishing Journal of Physics A: Mathematical and Theoretical

J. Phys. A: Math. Theor. **47** (2014) 105501 (24pp) doi:10.1088/1751-8113/47/10/105501

Unsteady immiscible multiphase flow validation of a multiple-relaxation-time lattice Boltzmann method

S Leclaire, N Pellerin, M Reggio and J-Y Trépanier

Department of Mechanical Engineering, École Polytechnique, 2500, chemin de Polytechnique, Montreal, Quebec, H3T 1J4, Canada

E-mail: sebastien.leclaire@polymtl.ca

Received 9 September 2013, revised 12 January 2014
Accepted for publication 16 January 2014
Published 19 February 2014

Abstract

The lattice Boltzmann modeling of immiscible multiphase flows needs to be further validated, especially when density variation occurs between the different flow phases. From this perspective, the goal of this research is to introduce the multiple-relaxation-time operator into a lattice Boltzmann model in order to improve its numerical stability in the presence of large density and viscosity ratios. Essentially, this research shows that the introduction of this operator greatly improves the numerical stability of the approach compared to the original single-relaxation-time collision operator. In many lattice Boltzmann research studies, multiphase lattice Boltzmann methods are validated using a reduced number of test cases, and unsteady flow test cases are frequently omitted before much more complex flow configurations are simulated. In this context, several test cases are proposed to evaluate the behavior of a lattice Boltzmann method for simulating immiscible multiphase flows with high density and viscosity ratios. These are: (1) two-phase Couette flow; (2) three-phase Laplace law; (3) three-phase Zalesak disk; (4) two-phase flow between oscillating plates; (5) two-phase capillary wave; and (6) the two-phase oscillating cylindrical bubble. The first two involve a steady regime, and the remaining four an unsteady regime.

Keywords: particle methods and lattice-gas methods in fluid mechanics, multiphase flows, incompressible viscous fluids, lattice Boltzmann method
PACS numbers: 02.60.Cb, 02.70.Ns, 47.55.Ca, 47.55.Hd, 47.35.Pq, 47.11.Qr
Mathematics Subject Classification: 76M28, 76T30, 76T10, 74S30, 65M99, 76D99

(Some figures may appear in colour only in the online journal)

 © 2014 IOP Publishing Ltd Printed in the UK

1. Introduction

The lattice Boltzmann (LB) method appeals to many researchers interested in fluid flow simulation. Its simplicity of application in the face of the complexity of the problems that it can address is one of the reasons for its substantial growth in popularity. One type of complex application is related to the simulation of immiscible multiphase flows. In this connection, the LB method for immiscible multiphase flows can be classified in the following categories:

– RK (Rothman and Keller) [1, 2];
– Shan and Chen [3];
– free-energy from Swift *et al* [4];
– mean-field from He *et al* [5]; and
– field-mediator from Santos *et al* [6].

Note that this list may not be exhaustive. Even though the LB method for the simulation of immiscible fluid flows is increasing in popularity, all the approaches developed require further validation. Here, we focus on the unsteady flow validation of an RK-type LB model to verify whether or not it can successfully address some basic multiphase flow test cases.

We begin with a brief review of the development of the RK model. Gunstensen *et al* [2] proposed the first LB model for the simulation of immiscible multiphase flow based on the RK lattice-gas model of Rothman and Keller [1]. Later, Grunau *et al* [7] modified the isothermal sound speed and relaxation coefficient in the model to permit variable density and viscosity between the phases. However, this model was stable only for small density ratios. Reis and Phillips [8] adapted this model for the popular D2Q9 lattice discretization. They also changed the perturbation operator, which introduces the surface tension, so that the operator complies with the capillary tensor within the macroscopic limit. Recently, Liu *et al* [9] have adapted the Reis and Phillips perturbation operator for the D3Q19 lattice.

Tölke [10] and Latva-Kokko and Rothman [11] have proposed changing the original recoloring operator of the model, because there were numerical artifacts in the model, such as spurious current and lattice pinning. By recoloring the color-blind distribution functions in a more symmetrical way, the number of these artifacts was greatly reduced. In fact, Leclaire *et al* [12] adapted the recoloring operator of Latva-Kokko and Rothman [11] for the Reis and Phillips model [8] and showed substantial improvement in the maximal density variation that the model could simulate in some test cases, i.e. up to $O(80)$. The new recoloring algorithm can also control the interface thickness, which makes it possible to avoid numerical problems and improve the scheme's stability [13, 14]. These recoloring algorithms were also modified for the simulation of flows with more than two phases [14–16], where the static contact angle at equilibrium can be controlled for high density and viscosity ratios [14]. Another study by Li *et al* [17] has proposed changing the recoloring step with a diffusion process. This is to account for the overly antidiffusion action of the original recoloring algorithm of Gunstensen *et al* [2]. Recently, Riaud *et al* [18] have introduced the Latva-Kokko and Rothman [11] recoloring operator into an Shan and Chen model, in order to improve the algorithm's stability while enforcing a constant interface thickness.

Isotropic color gradients have also been introduced into an RK model by Leclaire *et al* [13], who achieved accurate simulations with density ratios of $O(10\,000)$ for the Laplace law. In another study, Leclaire *et al* [14] changed the definition of the color gradient to improve the simulation of multiple immiscible fluids. In the latter, simultaneous density and viscosity ratios of $O(1000)$ and $O(100)$ respectively were obtained for several steady flow test cases with zero momentum.

In their work, the authors of [12, 14, 19] realized that the RK model formulation could not correctly simulate flow with density variation in the presence of non-zero momentum. This is called the discontinuity problem [20]. Lately, this problem has been partially solved with two methods, one incorporating special forcing terms [21] and the other including enhanced equilibrium distribution functions [22]. With the latter approach, it is shown that the model is able to simulate density and viscosity ratios in the steady Couette flow up to $O(1000)$ and $O(100)$ respectively. For an unsteady test case, the approach with the enhanced equilibrium distribution functions provides a stable simulation for an oscillating bubble up to a $O(100)$ density ratio. The numerical frequency of the bubble was compared to that of the analytical frequency, and this modification is found to greatly increase the accuracy of the model.

This brings us to the main subject of this study. With the exception of the recent study of Li *et al* [17], all the earlier RK models mentioned above have used the standard single-relaxation-time (SRT) single-phase collision operator. The goal of this research is to introduce the multiple-relaxation-time (MRT) operator into the model of [22], in order to improve its numerical stability in the presence of large density and viscosity ratios. In previous LB models with MRT in other immiscible multiphase flow categories, it has been found that there is enhanced numerical stability for high density and viscosity ratios [23]. With the Shan and Chen approach and MRT, Kuzmin and Mohamad [24] obtained an increase in the maximal density ratio from $O(100)$ to $O(160)$. Recently, Fakhari and Lee [25] extended an LB model with MRT to simulate high Reynolds numbers, and Schmieschek *et al* [26] have improved the accuracy of simulations in porous media with an Shan and Chen model incorporating the MRT operator. A 3D multiphase flow MRT model has also been developed by Premnath and Abraham [27]. The MRT model of Yu and Fan [28] has also been able to reduce the lowest stable viscosity by an order of magnitude compared to SRT. Chai and Zhao have extended the Chapman–Enskog analysis to the MRT model [29].

It has previously been shown that, with the SRT operator, the color-blind distribution functions of the proposed model recover the Navier–Stokes equations with weak pressure gradients and within small Mach and Knudsen number limits [22] at the small cost of introducing new, lower order error terms [30]. These new error terms improve the Galilean invariance of the original model, but this invariance is not completely restored. The analysis of the MRT model in [31] argues that, under the hypothesis that the hydrodynamic modes behave in exactly the same way as those of the linearized Navier–Stokes equations, the LB model is adequate to simulate the Navier–Stokes equations up to a certain order, as long as Galilean invariance is also ensured up to the same order. We argue that the MRT does not affect the order of the Galilean invariance of the model, and so the 'status' of the continuum limit and the equation of state of the model with MRT would be equivalent as that with the SRT model of [22]. A Chapman–Enskog analysis for MRT, such as the one performed in [29], would still be interesting to conduct, in order to validate further the macroscopic equations.

One of the advantages of the RK approach is the flexibility with which the model parameters can be chosen. All RK models allow independent control of the surface tension, the density ratio, and the ratio of viscosity of different fluids on both sides of the interface [32]. Recent RK models also allow the interface thickness to be controlled. Apart from the fact that the interface is diffuse, there is no violation of immiscibility, i.e. the interface thickness does not increase over time. The three-phase static contact angles can be automatically controlled by the various surface tension forces with high density and high viscosity ratios [14]. Moreover, control of the static contact angle on the wetting behavior of the solid phase is also possible with the RK model. Finally, droplet motion has been improved in recent work, through contact angle hysteresis [33].

This paper is organized as follows. First, the LB model for immiscible multiphase flow with the MRT operator is presented. Then, a number of numerical test cases are undertaken to validate the model's behavior in the presence of high density and viscosity ratios. Two steady multiphase flow test cases, namely the two-phase Couette flow and the three-phase Laplace law, are presented to show the enhanced stability of the MRT formulation compared to the SRT formulation. Four unsteady multiphase flow test cases follow: the three-phase Zalesak disc, the two-phase flow between oscillating plates, the two-phase capillary wave, and the two-phase oscillating cylindrical bubble. These are used to evaluate the ability of our current model to simulate unsteady flow with high density and/or viscosity ratios. Overall, this study shows that the model with the MRT operator is able to simulate simultaneous high density and/or viscosity ratios for unsteady flows in benchmark configurations.

2. Lattice Boltzmann immiscible multiphase model

The current LB approach follows the two-phase model of [8], along with the improvements presented in [12–14, 22] for the recoloring operator, the isotropic color gradient, the model generalization to N-phase flows, and the enhanced equilibrium distribution functions. The model presented here is an improvement over with the one in [22], because of the introduction of the MRT operator, a modification that brings about significant benefits. For this 2D LB model, there are N sets of distribution functions, one for each fluid, moving on a D2Q9 lattice with the velocity vectors $\vec{c_i}$. With $\theta_i = \frac{\pi}{4}(4-i)$, these velocity vectors are defined as follows:

$$\vec{c_i} = \left[c_i^x, c_i^y\right] = \begin{cases} [0,0], & i=1 \\ [\sin(\theta_i), \cos(\theta_i)]c, & i=2,4,6,8 \\ [\sin(\theta_i), \cos(\theta_i)]\sqrt{2}c, & i=3,5,7,9 \end{cases} \tag{1}$$

where $c = \Delta x/\Delta t$, $\Delta y = \Delta x$, Δx is the lattice spacing, and Δt is the time step.

The distribution functions for a fluid of color k (e.g. $k = r$ for red, $k = g$ for green, and $k = b$ for blue) are denoted $N_i^k(\vec{x}, t)$, while $N_i(\vec{x}, t) = \sum_k N_i^k(\vec{x}, t)$ is used for the color-blind distribution function. The evolution equation for the algorithm is the following:

$$|N^k(\vec{x} + \vec{c_i}\Delta t, t + \Delta t)\rangle = |N^k(\vec{x}, t)\rangle + \Omega^k(|N^k(\vec{x}, t)\rangle) \tag{2}$$

where the symbol $|.\rangle$ denotes a column vector expansion with respect to the velocity space, i.e. an expansion relative to the index i. For example, $|N^k\rangle = [N_1^k, N_2^k, \ldots, N_9^k]^T$, where T is the transpose operator. Similarly, the symbol $\langle .|$ denotes a row vector expansion with respect to the velocity space. This is the bra-ket Dirac notation. The collision operator Ω^k is the result of combining three sub operators (similar to [10]):

$$\Omega^k = (\Omega^k)^{(3)}[(\Omega^k)^{(1)} + (\Omega^k)^{(2)}]. \tag{3}$$

These original operators are rewritten in such a way that the evolution equation is solved in four steps with operator splitting, as follows.

(i) Single-phase collision operator:
$|N^k(\vec{x}, t_*)\rangle = (\Omega^k)^{(1)}(|N^k(\vec{x}, t)\rangle)$,

(ii) multiphase collision operator (perturbation):
$N_i^k(\vec{x}, t_{**}) = \left(\Omega_i^k\right)^{(2)}\left(N_i^k(\vec{x}, t_*)\right)$,

(iii) multiphase collision operator (recoloring):
$N_i^k(\vec{x}, t_{***}) = \left(\Omega_i^k\right)^{(3)}\left(N_i^k(\vec{x}, t_{**})\right)$,

(iv) streaming operator:
$N_i^k(\vec{x} + \vec{c_i}\Delta t, t + \Delta t) = N_i^k(\vec{x}, t_{***})$.

Because of the notation adopted for the MRT operator, the single-phase collision operator applies on the whole distribution function set $|N^k\rangle$, rather than on each N_i^k individually, as is the case with the other operators.

It is important to point out that, from the programming point of view, there is no need to use one set of distribution functions for each fluid k. Only the distribution functions of the color-blind fluid $N_i(\vec{x}, t)$ and each density field are required [14]. Considering this fact can greatly increase the efficiency of the model implementation.

2.1. Single-phase collision operator

The first sub operator, $(\Omega^k)^{(1)}$, is the MRT operator of the single-phase LB model, first developed in [34]. The distribution functions are relaxed towards a local equilibrium, in which $\mathbf{K}$ denotes a diagonal matrix of relaxation coefficients, and $\mathbf{M}$ is the matrix that shifts domain from distribution space to moment space:

$$(\Omega^k)^{(1)}(|N^k\rangle) = |N^k\rangle - \mathbf{M}^{-1}\mathbf{K}\mathbf{M}(|N^k\rangle - |N^{k(e)}\rangle). \tag{4}$$

Below are the details of this operator. The density of the fluid k is given by the first moment of the distribution functions:

$$\rho_k = \sum_i N_i^k = \sum_i N_i^{k(e)} \tag{5}$$

where the superscript (e) denotes equilibrium. The total fluid density is given by $\rho = \sum_k \rho_k$, while the total momentum is defined as the second moment of the distribution functions:

$$\rho\vec{u} = \sum_i \sum_k N_i^k \vec{c}_i = \sum_i \sum_k N_i^{k(e)} \vec{c}_i, \tag{6}$$

in which $\vec{u}$ is the velocity of the color-blind distribution functions. The equilibrium functions are defined by [22]:

$$N_i^{k(e)}(\rho_k, \vec{u}, \alpha_k) = \rho_k \left(\phi_i^k + W_i \left[\frac{3}{c^2}(\vec{c}_i \cdot \vec{u}) + \frac{9}{2c^4}(\vec{c}_i \cdot \vec{u})^2 - \frac{3}{2c^2}(\vec{u} \cdot \vec{u}) \right] \right) + \Phi_i^k. \tag{7}$$

The weights W_i are those of a standard D2Q9 lattice:

$$W_i = \begin{cases} 4/9, & i = 1 \\ 1/9, & i = 2, 4, 6, 8 \\ 1/36, & i = 3, 5, 7, 9. \end{cases} \tag{8}$$

Besides,

$$\phi_i^k = \begin{cases} \alpha_k, & i = 1 \\ (1 - \alpha_k)/5, & i = 2, 4, 6, 8 \\ (1 - \alpha_k)/20, & i = 3, 5, 7, 9. \end{cases} \tag{9}$$

As established in [7] for two-phase flows, the various density ratios between fluids k and l are γ_{kl}, and must be taken as follows to obtain a stable interface:

$$\gamma_{kl} = \frac{\rho_k^0}{\rho_l^0} = \frac{1 - \alpha_l}{1 - \alpha_k}, \tag{10}$$

where the superscript '0' over ρ_k^0 indicates the initial value of ρ_k at the beginning of the simulation.

The pressure of the fluid of color k is:

$$p_k = \rho_k \frac{3(1 - \alpha_k)}{5} c^2 = \rho_k \left(c_s^k\right)^2. \tag{11}$$

In the above expressions, one α_k is a free parameter. We let κ be the index of the least dense fluid. Generally, we set the value of $\alpha_\kappa > 0$ so that the relation $0 < \alpha_\kappa \leqslant \alpha_k < 1$ is guaranteed to hold for each fluid k. These parameters set the isothermal sound speed c_s^k in each fluid of color k. If the value of α_κ is set to 4/9, the isothermal sound speed in the model recovers the usual value of $c/\sqrt{3}$ when the density ratio between the fluids is unity.

As in [35], the following orthogonal moment set is chosen:

$$\mathbf{M} = \begin{bmatrix} \langle 1| \\ \langle c^x| \\ \langle c^y| \\ 3\langle c^x| \circ \langle c^x| + 3\langle c^y| \circ \langle c^y| - 4\langle 1| \\ \langle c^x| \circ \langle c^x| - \langle c^y| \circ \langle c^y| \\ \langle c^x| \circ \langle c^y| \\ -3\langle c^x| \circ \langle c^x| \circ \langle c^y| + 2\langle c^y| \\ -3\langle c^x| \circ \langle c^y| \circ \langle c^y| + 2\langle c^x| \\ 9\langle c^x| \circ \langle c^x| \circ \langle c^y| \circ \langle c^y| - 6\langle c^x| \circ \langle c^x| - 6\langle c^y| \circ \langle c^y| + 4\langle 1| \end{bmatrix} \tag{12}$$

where the symbol $\circ$ stands for the Hadamard product. The elements of the diagonal matrix $\mathbf{K}$ are the relaxation factors. If all the elements in $\mathbf{K}$ are identical, the scheme proposed here becomes an SRT operator, and this multiphase flow model is reduced to the one presented in [22]. The coefficients $K_{5,5}$ and $K_{6,6}$ are related to the bulk and shear stress, so their values are set to the usual effective relaxation parameter ω_{eff}. For this study, the other relaxation parameters in the diagonal matrix $\mathbf{K}$ are set to $\eta\omega_{\text{eff}}$ with $\eta = \frac{4}{5}$. The value η can also be viewed as a viscous damping coefficient. When the value of this coefficient is 1, the SRT scheme is recovered. By lowering its value, the other modes in the system are damped, and this action can stabilize the numerical scheme. At the extreme, where $\eta = 0$, all modes, except the fifth and sixth, are infinitely viscous. We find that, for the test cases in this research, a value of $\eta = \frac{4}{5}$ improves the stability of the model sufficiently, while at the same time maintaining an adequate level of accuracy. Note that the value $\eta = \frac{4}{5}$ is not expected to be universal. However, it seems to work well for all the test cases studied in this research.

The effective relaxation parameter ω_{eff} is defined so that the evolution equation, equation (2), respects the macroscopic equations for a single-phase flow in the single-phase regions. When the viscosities of the fluids are different, an interpolation is applied to define the parameter ω_{eff} at the interface.

As in [14], we define the bar functional as the density-weighted q average. For example, for a variable X_k defined for each fluid k, the density-weighted q average of this variable is defined as:

$$\overline{X}|_q = \begin{cases} \left(\sum_k \dfrac{\rho_k (X_k)^q}{\rho} \right)^{\frac{1}{q}}, & q \neq 0 \\ \left(\prod_k (X_k)^{\rho_k} \right)^{\frac{1}{\rho}}, & q = 0. \end{cases} \tag{13}$$

If ν_k is the kinematic viscosity of the fluid k, then, depending on the q average, one possible choice for the effective relaxation parameter is:

$$\omega_{\text{eff}} = \frac{2c^2 \Delta t}{6(\overline{\nu}|_q) + c^2 \Delta t}. \tag{14}$$

Depending on test the case, different values for q are used to interpolate the viscosity $\overline{\nu}|_q$ of the fluid. For the simulation of multiphase flows of different viscosities, a widely used

approximation is the interpolation of the viscosity at the interface [7, 14, 36, 37]. The two most common choices for viscosity interpolation are the expressions with $q = 1$ and $q = -1$, which lead to the two following simplified expressions:

$$\overline{\nu}|_{q=0} = \sum_k \frac{\rho_k}{\rho} \nu_k, \tag{15}$$

$$\overline{\nu}|_{q=-1} = \frac{\rho}{\sum_k \frac{\rho_k}{\nu_k}}. \tag{16}$$

Finally, from [22], the expression for Φ_i^k in equation (7) is defined such that:

$$\Phi_i^k = \begin{cases} -3\overline{\nu}|_q(\vec{u} \cdot \vec{\nabla}\rho_k)/c^2, & i = 1 \\ +4\overline{\nu}|_q(\mathbf{G}_k : \vec{c}_i \otimes \vec{c}_i)/c^4, & i = 2, 4, 6, 8 \\ +1\overline{\nu}|_q(\mathbf{G}_k : \vec{c}_i \otimes \vec{c}_i)/c^4, & i = 3, 5, 7, 9 \end{cases} \tag{17}$$

where $\otimes$ is the tensor product and the symbol ':' stands for the tensor contraction. The tensor $\mathbf{G}_k$ is defined by:

$$\mathbf{G}_k = \frac{1}{8}\left[(\vec{u} \otimes \vec{\nabla}\rho_k) + (\vec{u} \otimes \vec{\nabla}\rho_k)^T\right]. \tag{18}$$

2.2. Perturbation operator

The surface tension in the RK model is modeled by means of the perturbation operator [2, 8]. To introduce surface tension into this model, a 'color' gradient $\vec{F}_{kl}$ would need to be defined first, which approximates the normal interface for each of the k-l fluid interfaces. The color gradient in this model is defined as:

$$\vec{F}_{kl} = \frac{\rho_l}{\rho}\vec{\nabla}\left(\frac{\rho_k}{\rho}\right) - \frac{\rho_k}{\rho}\vec{\nabla}\left(\frac{\rho_l}{\rho}\right). \tag{19}$$

For flow with three phases or more, this formulation for the color gradient has been shown to be superior to the usual RK color gradient [14].

The perturbation operator for the fluid k is therefore defined by:

$$\left(\Omega_i^k\right)^{(2)}\left(N_i^k\right) = N_i^k + \sum_{\substack{l \\ l \neq k}} \frac{A_{kl}}{2}|\vec{F}_{kl}|\left[W_i \frac{(\vec{F}_{kl} \cdot \vec{c}_i)^2}{|\vec{F}_{kl}|^2 c^2} - B_i\right] \tag{20}$$

with

$$B_i = \begin{cases} -4/27, & i = 1 \\ 2/27, & i = 2, 4, 6, 8 \\ 5/108, & i = 3, 5, 7, 9. \end{cases} \tag{21}$$

In [8], it was shown that the perturbation operator complies, within the macroscopic limit, with the capillary stress tensor present in the macroscopic equations for two-phase flows. It handles the coupling between the two fluids, with the space- and time-dependent parameters A_{kl} chosen to model the surface tension at the k-l fluid interface.

The surface tension σ_{kl} is set as follows:

$$\sigma_{kl} = \frac{1}{9}\frac{(A_{kl} + A_{lk})}{\omega_{\text{eff}}}c^2. \tag{22}$$

The values for σ_{kl} are set at the beginning of a simulation. However, the values for $A_{kl} = A_{lk}$ are space- and time-dependent, because ω_{eff} may depend on space and time.

Although this operator generates the surface tension, it does not guarantee the fluid's immiscibility. To minimize the mixing and segregate the fluids, the recoloring operator $(\Omega_i^k)^{(3)}$ needs to be properly selected.

2.3. Recoloring operator

This operator is used to maximize the amount of fluid of color k at the interface that is sent to the k fluid region, while respecting the laws of conservation of mass and total momentum. The recoloring operator presented here is a combination of the essential ideas presented in [11, 15], and is as follows:

$$\left(\Omega_i^k\right)^{(3)}\left(N_i^k\right) = \frac{\rho_k}{\rho} N_i + \sum_{\substack{l \\ l \neq k}} \beta_{kl} \frac{\rho_k \rho_l}{\rho^2} \cos\left(\varphi_i^{kl}\right) N_i^{(e)}(\rho, 0, \overline{\alpha}|_{q=1}), \tag{23}$$

where β_{kl} is a parameter controlling the thickness of the k-l interface. The variable φ_i^{kl} corresponds to the angle between the color gradient $\vec{F}_{kl}$ and the lattice velocity $\vec{c_i}$. The equilibrium distributions of the color-blind fluid $N_i^{(e)}$ in equation (23) are evaluated using equation (7), a zero velocity, and the respective value of $\overline{\alpha}|_{q=1}$.

2.4. Other details

Isotropic discrete gradient operators are used for the discretization of the gradients in equations (17) and (19). This kind of gradient discretization, which was generalized in [38] for 2D and 3D space, enhances the accuracy of the RK model significantly [13]. To compute this type of gradient efficiently, convolution products can be used, as explained in [39].

For three-phase flows, and when the surface tension yields a Neumann triangle, there is a possible equilibrium state where static contact angles will be formed between the fluids. To bring these angles to equilibrium, a special expression for β_{kl} should be used [14, 16]. In this study, these special relations are not used, and each β_{kl} is set to the same constant.

3. Numerical simulation

In this work, the figures with colors showing multiphase flow are RGB images of size $N_x \times N_y \times 3$ given by:

$$RGB = \frac{\left[\frac{\rho_r}{\rho_r^0}, \frac{\rho_g}{\rho_g^0}, \frac{\rho_b}{\rho_b^0}\right]}{\sum_k \frac{\rho_k}{\rho_k^0}} \tag{24}$$

where N_x and N_y denote the number of lattice sites in the horizontal and vertical directions. Also, in the tables below, the letter `D` stands for density ratio, and `V` stands for the viscosity ratio. All the **unsteady** flow simulations presented in this research were run with the MRT collision operator. In fact, in each of the unsteady flow simulations, the SRT operator leads to instability and divergence of the numerical simulation for the simulation parameters chosen. Table 1 shows some simulation parameters corresponding to different test case sections. Note that the parameter $\alpha_\kappa = 4/9$ is constant in this work (κ index of the least dense fluid).

3.1. Steady flow: two-phase Couette flow

The first numerical test in this study is the standard two-phase Couette flow. This flow consists of two layers of fluid moving in a channel between two parallel moving plates. Usually, the goal of this test case is to attest the model's ability to simulate a shear flow with variable dynamic viscosity between the phases. Several RK models [7–10, 12–14], as well as other LB models [19], are not able to capture the theoretical momentum discontinuity of this flow in the presence of density ratios. This is known as the discontinuity problem of the multiphase LB method [20]. In fact, this test case is very simple to set up, and should be a must for researchers

Table 1. Simulation parameters for the various test cases. If a parameter is marked with the symbol '-', it means either that it is not required or that it is defined in the corresponding section.

	Test case section					
	(3.1)	(3.2)	(3.3)	(3.4)	(3.5)	(3.6)
N_x	160	128	200	–	–	–
N_y	1	128	200	–	–	–
Δx	1	1	1	$31/(N_x - 1)$	1	1
Δy	–	1	1	–	1	1
Δt	1	1	1	Δx^2	1	1
u_0^y	0.0001	–	–	$-10^{-4}\sin(2\pi 10^{-3}t)$	–	–
u_N^y	−0.01	–	–	$+10^{-4}\sin(2\pi 10^{-3}t)$	–	–
β_{kl}	0.8	0.5	0.7	0.8	1	1
q	−1	1	1	–	–	–
ρ_b^0	1	1	1	1	1/100	1/100
ν_r	1/2	1	1	1	1/1000	1/250
ν_b	–	–	–	–	1/1000	1/250
σ_{rb}	0	8E-02	0	0	10E-05	10E-05
σ_{rg}	–	8E-02	0	–	–	–
σ_{gb}	–	4E-01	0	–	–	–
$(\Omega^k)^{(1)}$	–	–	MRT	MRT	MRT	MRT
F_{kl}	[22]	[14]	[14]	[22]	[22]	[14]

Table 2. Additional simulation parameters for the two-layered Couette flow.

Case	Type	ρ_r^0/ρ_b^0	ν_r/ν_b
(3.1 a)	D1−V1	1	1
(3.1 b)	D20−V20	20	20
(3.1 c)	D1000−V100	1000	100
(3.1 d)	D1000−V150	1000	150
(3.1 e)	D5000−V5000	5000	5000

to consider in LB multiphase modeling. Various authors have proposed solutions to deal with this problem [30, 40–42], applying different methodologies. Recently, new formulations using appropriate source terms or enhanced equilibrium distributions have been proposed for RK models, which are designed to capture the momentum discontinuity with variable density ratios [21, 22]. Here, we apply the enhanced equilibrium distribution approach to correctly simulate these ratios. Note that two-phase Couette flow with the SRT formulation has already been studied by Leclaire *et al* [22]. Nevertheless, for the purposes of this study, this numerical test is used to compare the stability between the SRT and the MRT LB formulation. For clarity, we have taken the setting of the test from [22], and will clearly show that the MRT formulation leads to a much more stable numerical scheme. The details of the test are the same as in [22], but with the parameters given in table 1. Table 2 also provides additional simulation parameters for different simulation cases.

As previously explained by Leclaire *et al* [14], the initial condition for this problem can lead to instability, because the color-blind density distribution N_1 and the fluid densities ρ_k are initially discontinuous. In this case, it is preferable to initialize the flow with a more continuous function. To do so, the model equations are solved for a certain number of time steps with $A_{kl} = 0$, while $\vec{u} = 0$ is imposed in the equilibrium density distribution in equation (7). Thus, for the simulations presented here, the first 2000 time steps serve only to stabilize the initial

Table 3. Errors in the norm L^1 between the theoretical and numerical momentum profiles for the two-phase Couette flow.

		Error $= \dfrac{\sum_j \left\lvert (\rho u^y)(x_j)\lvert_{\text{the}} - (\rho u^y)(x_j)\lvert_{\text{num}} \right\rvert}{N_x - 1}$	
Case	Type	SRT	MRT
(3.1 a)	D1−V1	1.06E-07	1.06E-07
(3.1 b)	D20−V20	9.29E-05	9.29E-05
(3.1 c)	D1000−V100	6.80E-04	6.72E-04
(3.1 d)	D1000−V150	N/A	6.73E-04
(3.1 e)	D5000−V5000	N/A	2.90E-03

density distribution and fluid densities to yield a more continuous function. It is important to mention that this initial smoothing does not always work as we would wish. In some situations, it may be better not to smooth the initial condition.

Note that the numerical steady state is regarded as achieved when:

$$\max_{\text{all sites}} \left\{ \left| \frac{(N_i)^{(n)} - (N_i)^{(n-1)}}{(N_i)^{(n)}} \right| \right\} \leqslant \epsilon \tag{25}$$

with $\epsilon = 10^{-10}$, while n denotes the time step number. To reduce the computational cost, this condition is only checked at every 2000 time steps.

Table 3 shows the errors of the momentum profiles in norm L^1 for different simulation cases. For both the SRT and MRT formulations, the error increases as the density and viscosity ratios increase, and the accuracy of the two operators is similar. What is interesting to note is that the MRT approach allows the simultaneous simulation of density and viscosity ratios up to $O(5000)$. Note that, with the current setting, this corresponds to a ratio of $O(25\,000\,000)$ in terms of the dynamic viscosity. The SRT formulation is limited to $O(1000)$ for the density ratio, and $O(150)$ for the viscosity ratio. It is clear that the MRT approach extends the stability significantly, and consequently the range of valid parameters of the method. This test case clearly indicates the superiority of the MRT approach. However, it is important to undertake more complex flow configurations to claim that our conclusion is definitive.

3.2. Steady flow: three-phase Laplace law

The main goal in this next investigation is again to compare the stability of the SRT formulation to that of the MRT formulation, but, in a intricate flow situation, i.e. with an unsteady flow regime, curved interfaces, triple fluid junctions, and non-zero surface tension, as well as high density ratios and high viscosity ratios. The three-phase Laplace law test was introduced in [14]. Initially, this test was developed to ensure that the scheme does not break the Laplace law in the presence of three fluids. Overall, this test case has four main purposes. The first is to check the stability of the numerical scheme. The second is to check the qualitative evolution of the flow. The third is to use an analytical solution to relate the different surface tensions and the pressure jump at the interfaces at steady state. This is similar to the more traditional two-phase Laplace law [13]. The fourth is to compare the intensity of the spurious currents obtained with the SRT and MRT operators. The details of the test are the same as in [22], but with the parameters given in table 1. Table 4 also shows the additional simulation parameters for the various simulation cases. As described in section (3.1), the initial condition of this problem can lead to instability. Therefore, the first 2000 time steps are used to stabilize that condition. Also, the numerical steady state is regarded as achieved with $\epsilon = 10^{-7}$. Some

Table 4. Additional simulation parameters for the three-phase Laplace law tests.

Case	Type	ρ_r^0/ρ_b^0	ρ_g^0/ρ_b^0	ν_r/ν_b	ν_g/ν_b
(3.2 a)	D1−V1	1	1	1	1
(3.2 b)	D20−V20	20	$\sqrt{20}$	20	$\sqrt{20}$
(3.2 c)	D1000−V100	1000	$\sqrt{1000}$	100	$\sqrt{100}$
(3.2 d)	D1000−V350	1000	$\sqrt{1000}$	350	$\sqrt{350}$
(3.2 e)	D2000−V2000	2000	$\sqrt{2000}$	2000	$\sqrt{2000}$

Table 5. Spurious currents and relative errors in % for the three-phase Laplace law tests.

		$\lvert\vec{u}\rvert_{\max}$		Error (%)	
Case	Type	SRT	MRT	SRT	MRT
(3.2 a)	D1−V1	1.56E-03	2.20E-03	5.44	4.27
(3.2 b)	D20−V20	4.89E-04	8.44E-04	0.68	0.39
(3.2 c)	D1000−V100	3.98E-04	7.19E-04	4.02	2.41
(3.2 d)	D1000−V350	N/A	8.72E-04	N/A	2.23
(3.2 e)	D2000−V2000	N/A	1.04E-03	N/A	2.16

simulations did not converge under the prescribed stopping criterion, so we stopped them after 5000 000 time steps. The quantity of interest, namely the spurious currents or the three-phase Laplace law error, had converged much earlier, and this allowed us to compare the behavior of the SRT and MRT operators in terms of the final steady state accuracy.

At steady state, if the Laplace law for two-phase flow is applied iteratively across the two interfaces *r*-*g* and *r*-*b*, we should obtain the following result [14]:

$$\sigma_{rg} + \sigma_{rb} = \Delta P_{gr} R_g + \Delta P_{rb} R_r \tag{26}$$

where $\Delta P_{gr} = P_g - P_r$ and $\Delta P_{rb} = P_r - P_b$ indicate the pressure jumps across the various fluid interfaces. Also, R_g is the radius of the green circular bubble and R_r is the outer radius of the red fluid annulus at equilibrium. As in [14], the values ΔP_{gr}, ΔP_{rb}, R_g, and R_r are evaluated numerically and compared to the theoretical values. The left-hand side of equation (26) is used as the reference to calculate the relative errors.

Table 5 shows the spurious currents and the errors in % with the three-phase Laplace law for the various simulation cases. The spurious currents are of the same order for both operators, but slightly lower with the SRT operator. However, we note the enhanced stability of the MRT formulation compared to the SRT formulation. In fact, with MRT, simultaneous density and viscosity ratios up to $O(2000)$ can be achieved, while with SRT, the density and viscosity ratios are limited to $O(1000)$ and $O(350)$ respectively. It is also important to note that, even for the D2000−V2000 type, the MRT approach still has an error of only 2.16% with the three-phase Laplace law. As well, compared with the two-layered Couette flow, the maximum density and viscosity ratios are reduced. This is attributed to the flow configuration, which is much more complex with the three-phase Laplace law. Concerning the Laplace law error, for this test case, the MRT operator is slightly more accurate than the SRT operator.

Overall, the simulations show that the MRT formulation greatly enhances the stability of the scheme, while at the same time maintaining the accuracy of the three-phase Laplace law at high density and viscosity ratios. It should be noted that this three-phase Laplace law test case does not inspect the flow evolution of the unsteady regime quantitatively, but only checks its stability in that regime. So, the next step in this research was a quantitative analysis of the scheme's behavior in the unsteady regime.

Table 6. Additional simulation parameters for the three-phase Zalesak disc.

Case	Type	U_0	ρ_r^0/ρ_b^0	ρ_g^0/ρ_b^0	ν_r/ν_b	ν_g/ν_b
(3.3 a)	D1−V1	0.02	1	1	1	1
(3.3 b)	D1000−V1000	0.0002	1000	$\sqrt{1000}$	1000	$\sqrt{1000}$

3.3. Unsteady flow: three-phase Zalesak disc

The next test case in this study is derived from the well-known Zalesak disc test case [43]. However, for this research, the numerical setup has been adapted to three-phase flow, so that we can check the effect of the triple fluid junction on the flow qualitatively, as well as some quantitative unsteady flow behaviors with high density and viscosity ratios. Also, with this test case, we can study the incompressible limit of the current method.

Historically, this test case is usually used to evaluate the performance of interface tracking algorithms, such as the level-set method [44]. It was recently used by the LB community to evaluate the behavior of an LB interface tracking algorithm [45]. The results obtained by these authors are promising, as the theoretical contours of the various interface positions are well tracked.

It should be pointed out that the LB model proposed in this work is not itself an interface tracking algorithm, but rather a hydrodynamic multiphase flow solver. However, for the purposes of this research, it is still possible to extract important and pertinent information from this test case. In such a test, a theoretical velocity field $\vec{u}$ is imposed throughout the simulation in the equilibrium distribution in equation (7). For the current model, the interface (or color) positions should then move as predicted by that velocity field. This is because the surface tension effects are set to zero.

We now describe the simulation setting in the context of this LB model. We use a lattice of 200×200 sites placed over the computational domain $[1, 200] \times [1, 200]$. Periodic boundary conditions are used at the four ends. The fluids are initialized using the zero velocity equilibrium distribution functions. The following zones are defined:

$$Z_1 = \{(x, y) \in \mathbb{R}^2 : (x - 100.5)^2 + (y - 100.5)^2 < 80^2\}, \tag{27}$$

$$Z_2 = \{(x, y) \in \mathbb{R}^2 : x < 84.5\}, \tag{28}$$

$$Z_3 = \{(x, y) \in \mathbb{R}^2 : x < 100.5\}, \tag{29}$$

$$Z_4 = \{(x, y) \in \mathbb{R}^2 : y \leqslant 108\}, \tag{30}$$

$$Z_5 = \{(x, y) \in \mathbb{R}^2 : y \geqslant 93\}. \tag{31}$$

The superscript c indicates the complement for the sets. The red fluid is then initialized in the following zone: $Z_1^c \cup (Z_1 \cap Z_3^c \cap Z_4 \cap Z_5)$, while the blue fluid is initialized in the following zone: $Z_1 \cap Z_2^c \cap Z_3$. The remaining lattice sites are filled with green fluid. Table 7 illustrates the initial fluid color positions. The following velocity field is imposed:

- $u_x = -\pi U_0 (y - 100.5)/200$ (imposed x-velocity);
- $u_y = +\pi U_0 (x - 100.5)/200$ (imposed y-velocity).

Table 6 provides additional simulation parameters for the various simulation cases. As described in section (3.1), the initial condition of this problem can lead to instability. Therefore, the first 50 000 time steps are used to stabilize that condition.

Some of the results of these simulations are expected. First, the imposed velocity field induces a vortex around the axis perpendicular to the x–y-plane located at $x = 100.5$ and $y = 100.5$. Therefore, the contour of each density field, $\rho_k = \rho_k^0/2$, should then rotate with an angular velocity of $\omega_{\text{ang}} = \pi U_0/200$ around that axis. This means that the time required for one cycle to complete is equal to $t_{\text{cyc}} = 2\pi/\omega_{\text{ang}} = 400/U_0$. The position of the contours should then be in agreement with this angular velocity.

Table 7 presents our simulation results (3.3 a) and (3.3 b), which correspond to types D1−V1 and D1000−V1000 respectively. Note that $t^* = t/t_{\text{cyc}}$. The contours $\rho_k = \rho_k^0/2$ of each fluid are shown at $t^* = 0$, $t^* = 1/4$, $t^* = 2/4$, and $t^* = 3/4$. It is clear that, globally, the density fields rotate with the correct angular velocity for both types. This strongly suggests that the recoloring operator works well, and is able to recolor the color-blind density distributions with the right color and at the right position.

For both cases, an inspection of the six triple fluid junctions reveals that these junctions seem to locally perturb the position of the various density fields ρ_k. Also, the sharp angle of the initial flow configuration is smoothed out. With type D1000−V1000, some anisotropic deformations of the position of the contours seem to appear near the triple fluid junctions. These deformations are not present with type D1−V1.

In general, the flow follows the correct angular velocity, but locally, at the triple fluid junctions, some errors are introduced, and these could be the object of a deeper analysis. It should be noted that the surface tension effects are set to zero here. When these effects are not zero, this numerical method is able to recover the static contact angles predicted at the triple fluid junctions by the Laplace–Young law at equilibrium [14, 16].

This test case also allows us to determine the incompressible limit of the method. It has already been stated in a previous work [13] that the incompressible limit of this scheme is affected by the density ratios between the different phases. Effectively, in a simulation, the lattice Mach number, Ma, can be approximated by the following relation:

$$\text{Ma} = \frac{|\vec{u}|}{\sqrt{\frac{3}{5}(1 - \overline{\alpha}|_{q=1})c^2}}. \tag{32}$$

The maximum lattice Mach number throughout the simulation case (3.3 b) with type D1000−V1000 is computed as approximately equal to 0.024. An interesting test that we performed was to increase U_0 in the simulation case (3.3 b), and see up to what value the scheme is rendered unstable. This value seems to be around $U_0 = 0.0018$ for a maximum lattice Mach number of 0.22 during the simulation. At such a lattice Mach number, the LB model used in this work may be subject to instability. A value below 0.1 for the lattice Mach number is usually preferable, but a smaller value might even be necessary, in order to avoid the compressibility error of the LB method [46]. This indirectly suggests that the scheme could be stable for higher density and viscosity ratios, as long as the incompressible limit of the method is respected. This is not a proof, but it is an indication that the scheme could more stable if this incompressible limit could be relaxed or be less restrictive, or both. In other words, if a stable interface with density ratios between the different colors could be simulated without using a variable lattice speed of sound [7], this would increase the robustness of the method. Indeed, in the dense phase, the lattice speed of sound is inversely proportional to the square root of the density ratio [13]. Overall, this affects both the stability limit and the precision of this model.

This test case has provided interesting information on the unsteady behavior of the numerical approach. The next step is to test the scheme again with various unsteady test cases, where all the hydrodynamics equations are in action, as this would make it possible to extract quantitative data that will further validate this multiphase flow model.

Table 7. Three-phase Zalesak disc contours. (An interpretation of the references to color in this table can be found in the online version of this article.)

Contour	Case	Type	$t^* = 0$	$t^* = 1/4$	$t^* = 1/2$	$t^* = 3/4$
Fill	(3.3 a)	D1-V1	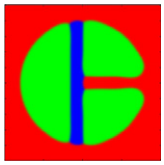	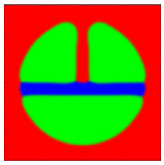	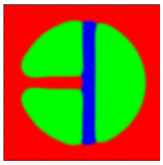	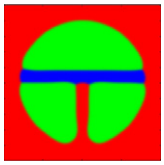
	(3.3 b)	D1000-V1000	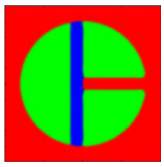	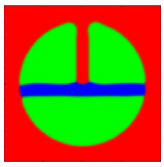	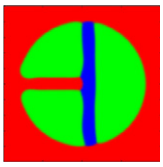	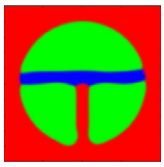
ρ_r	(3.3 a)	D1-V1	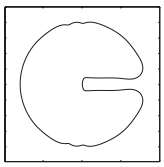	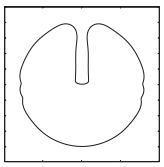	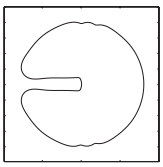	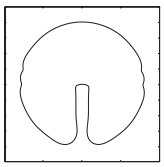
	(3.3 b)	D1000-V1000	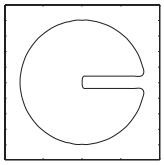	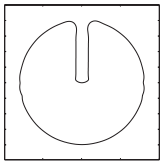	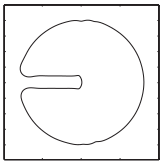	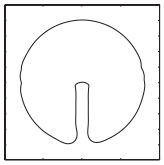
ρ_g	(3.3 a)	D1-V1	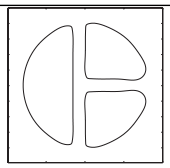	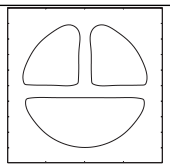	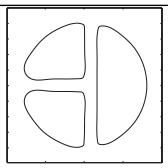	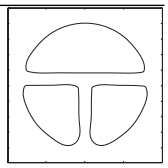
	(3.3 b)	D1000-V1000	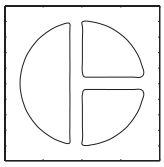	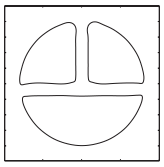	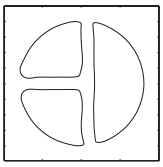	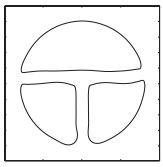
ρ_b	(3.3 a)	D1-V1	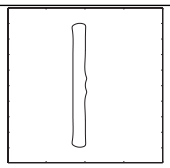	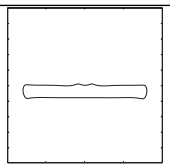	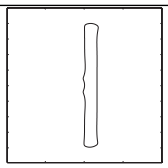	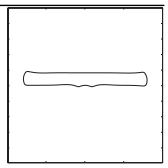
	(3.3 b)	D1000-V1000	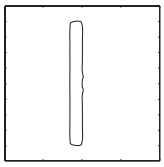	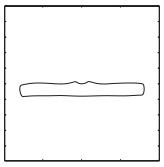	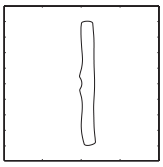	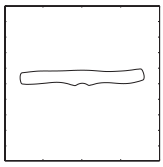

Table 8. Additional simulation parameters for the two-phase flow between oscillating plates.

Case	Type	ρ_r^0/ρ_b^0	ν_r/ν_b
(3.4 a)	D1−V1	1	1
(3.4 b)	D1−V100	1	100
(3.4 c)	D100−V100	100	100
(3.4 d)	D1000−V1000	1000	1000

3.4. Unsteady flow: two-phase flow between oscillating plates

The second unsteady test case studies the behavior of a two-phase stratified flow between two oscillating plates. The goal of the test is to check the model's ability to capture the theoretical maximal amplitude of the momentum profiles during the unsteady process of this two-phase flow. This kind of flow is important in terms of investigating flow-induced vibrations [47, 48]. For the purposes of this research, this test makes it possible to validate the behavior of the model for an unsteady shear flow combined with high density and viscosity ratios between the phases. It is similar to that of the two-phase Couette flow, but the flow is in an unsteady regime, because the velocities u_0^y and u_N^y of the plates are time-dependent. The authors believe that this flow may never have been studied by an LB model, and, if this is the case, it constitutes an interesting test case for LB multiphase flow modeling.

We first describe the setting of this test in the current context. A lattice of $N_x \times 1$ sites is used, and placed over the computational domain $[-31, 31]/2$. Unless otherwise stated, $N_x = 64$. The walls located at $x_0 = -31/2$ and $x_N = 31/2$ cover the lattice sites, while the interface $x_I = 0$ lies between the fluid lattice sites. Because the model is two-dimensional, periodic boundary conditions are applied in the y-direction. The velocity boundary conditions, in this case the standard Zou and He [49] velocity boundary condition, are implemented where the first and last sites are located. Table 8 provides additional simulation parameters for the various simulation cases.

The interpolation for the viscosity is not the usual q-average for these simulations. It appears that for this test, the results are much better when the following definition for fluid viscosity is used:

$$\overline{\nu}|_q = \begin{cases} \nu_r, & \rho_r > \rho_b \\ \nu_b, & \text{otherwise.} \end{cases} \tag{33}$$

Each fluid section is initialized with the zero velocity equilibrium distribution functions, but, as described in section (3.1), the initial condition of this problem can lead to instability. Therefore, the first 2000 time steps are used to stabilize that condition.

There is an analytical solution available for the momentum profiles when the analysis is based on the hypothesis of a small amplitude motion [47, 48]. Here, we describe the analytical solution in the context of this LB simulation. The channel half width is $H = (N_x - 1)\Delta x/2$, and $\hat{x} = x/H$ is the non-dimensional coordinate. Note that $\hat{x}_I = x_I/H = 0$ in our case. The non-dimensional reduced y-velocity $\hat{u}^y(\hat{x})$ is defined by:

$$\hat{u}^y(\hat{x}) = \frac{u^y(\hat{x}, t)}{U_0\, \mathrm{e}^{\mathrm{i}(2\pi f)t}} \tag{34}$$

and the solution for this reduced y-velocity is given by the following expression:

$$\hat{u}_k^y(\hat{x}) = C_{kb}\, \mathrm{e}^{\lambda_k \hat{x}} + C_{kr}\, \mathrm{e}^{-\lambda_k \hat{x}} \tag{35}$$

where the subscript k refers to r for the red fluid and to b for the blue fluid. The values $U_0 = 10^{-4}$ and $f = 10^{-3}$. The complex constant $\lambda_k = (1 + \mathrm{i})\sqrt{\mathrm{Re}_k/2}$, and the oscillatory

Table 9. Errors in the norm L^1 between the theoretical and the numerical normalized maximum momentum amplitude profiles for the two-phase flow between oscillating plates.

		$\text{Error} = \dfrac{\sum_j \left\lvert (\widehat{\rho u^y})(\hat{x}_j)\lvert_{\text{the}} - (\widehat{\rho u^y})(\hat{x}_j)\lvert_{\text{num}} \right\rvert}{N_x - 1}$				
Case	Type	$N_x = 32$	$N_x = 64$	$N_x = 96$	$N_x = 128$	Order
(3.4 a)	D1−V1	3.49E-03	8.61E-04	3.80E-04	2.13E-04	2.02
(3.4 b)	D1−V100	1.19E-02	2.92E-03	1.30E-03	7.33E-04	2.01
(3.4 c)	D100−V100	5.43E-02	2.51E-02	1.63E-02	1.21E-02	1.09
(3.4 d)	D1000−V1000	4.72E-02	2.42E-02	1.58E-02	1.16E-02	1.01

Reynolds number $\text{Re}_k = 2\pi f H^2/\nu_k$. The constants C_{kb} and C_{kr} are determined by the boundary and interface conditions, i.e. imposed velocities at the walls and a continuous velocity field at the interfaces. These latter lead to the following system of equations:

$$\begin{pmatrix} \mathrm{e}^{\lambda_b} & \mathrm{e}^{-\lambda_b} & 0 & 0 \\ \mathrm{e}^{\lambda_b \hat{x}_I} & \mathrm{e}^{-\lambda_b \hat{x}_I} & -\mathrm{e}^{\lambda_r \hat{x}_I} & -\mathrm{e}^{\lambda_b \hat{x}_I} \\ \lambda_b\, \mathrm{e}^{\lambda_b \hat{x}_I} & -\lambda_b\, \mathrm{e}^{-\lambda_b \hat{x}_I} & M_{33} & M_{34} \\ 0 & 0 & \mathrm{e}^{-\lambda_r} & \mathrm{e}^{\lambda_r} \end{pmatrix} \cdot \begin{pmatrix} C_{bb} \\ C_{br} \\ C_{rb} \\ C_{rr} \end{pmatrix} = \begin{pmatrix} 1 \\ 0 \\ 0 \\ -1 \end{pmatrix} \tag{36}$$

where:

$$M_{33} = -\frac{\text{Re}_b}{\text{Re}_r} \frac{\rho_r^0}{\rho_b^0} \lambda_r\, \mathrm{e}^{\lambda_r \hat{x}_I} \tag{37}$$

$$M_{34} = +\frac{\text{Re}_b}{\text{Re}_r} \frac{\rho_r^0}{\rho_b^0} \lambda_r\, \mathrm{e}^{-\lambda_r \hat{x}_I}. \tag{38}$$

We define the theoretical normalized maximum momentum amplitude as follows:

$$(\widehat{\rho u^y})(\hat{x})|_{\text{the}} = \begin{cases} \left|\rho_r^0 \hat{u}_r^y(\hat{x})\right|/\rho_r^0, & -1 \leqslant \hat{x} < \hat{x}_I \\ \left|\rho_b^0 \hat{u}_b^y(\hat{x})\right|/\rho_r^0, & +\hat{x}_I < \hat{x} \leqslant 1. \end{cases}$$

Note that here the symbol $|.|$ indicates the magnitude of a complex expression. The numerical normalized maximum momentum amplitude is computed with the following expression:

$$(\widehat{\rho u^y})(\hat{x})|_{\text{num}} = \frac{\rho}{c U_0 \rho_r^0} U_{\max}(\hat{x}), \tag{39}$$

where $U_{\max}(\hat{x})$ is the maximum value of $u^y(\hat{x}, t)$ during the simulation time interval $10\,000\Delta t \leqslant t \leqslant 20\,000/\Delta t$. The lower bound $10\,000\Delta t$ is set to guarantee that $U_{\max}$ is not affected by the initial condition.

Figure 1 compares the theoretical and numerical momentum amplitude profiles for the simulation cases (3.4 a−d). It is clear that the two profiles match very well, even with type D1000−V1000. The momentum discontinuity is about 5–6 lattice units in thickness. These are good results, and there are no overshoots.

Table 9 shows the errors in the norm L^1 for the different simulation cases, and the order of accuracy with respect to the analytical solution. A second-order accuracy is achieved only when the density ratio is unity. Otherwise, the order of accuracy of the scheme drops to 1. With a jump in the flow properties, it is possible to lose second-order convergence [50]. Although we have not investigated the issue, we believe that, at the moment, the most important point is that the model is compatible with this theoretical unsteady two-phase flow configuration.

As for the steady Couette flow, this test does not evaluate the performance of the scheme with curved interfaces and non-zero surface tension. The next test, with new complexities in the flow configuration, will address these issues.

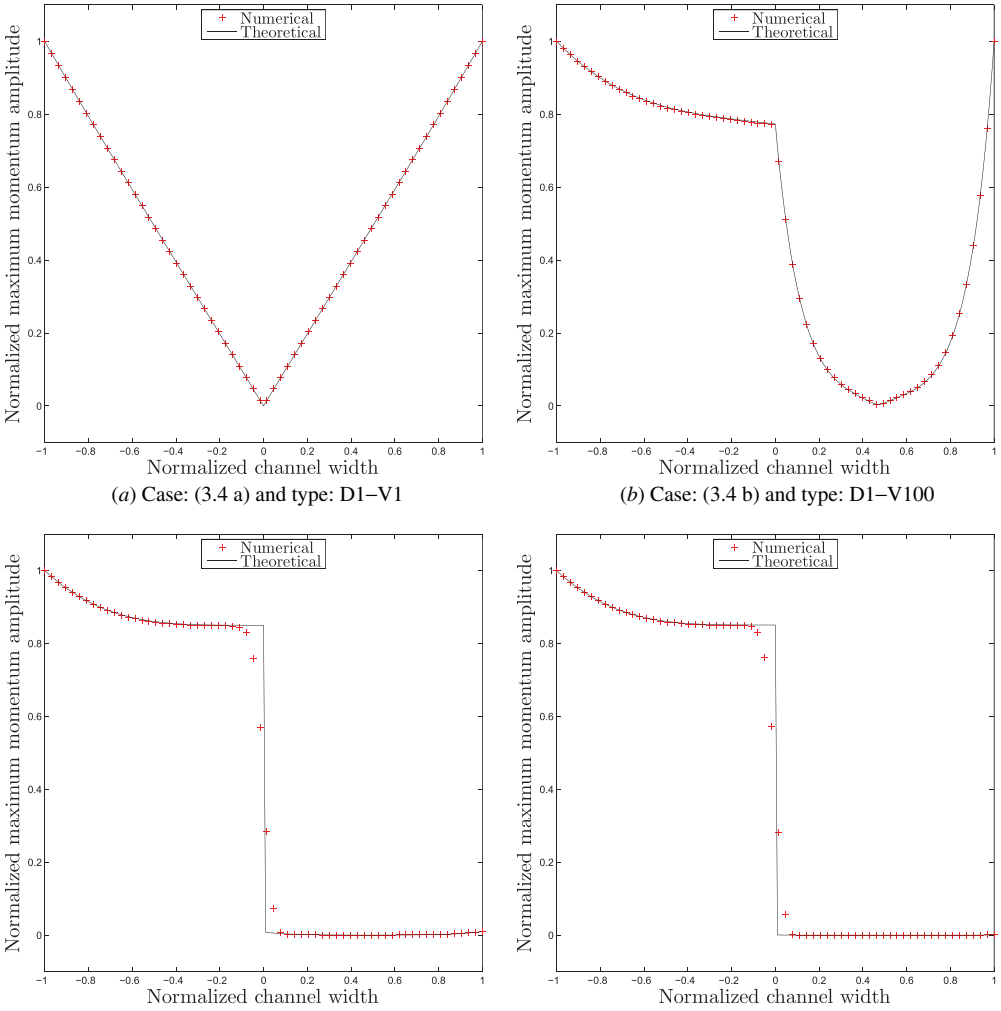

(*a*) Case: (3.4 a) and type: D1−V1

(*b*) Case: (3.4 b) and type: D1−V100

(*c*) Case: (3.4 c) and type: D100−V100

(*d*) Case: (3.4 d) and type: D1000−V1000

Figure 1. Theoretical and numerical normalized maximum momentum amplitude profiles for the two-phase flow between oscillating plates.

3.5. Unsteady flow: two-phase capillary wave

The capillary wave motion is a basic test case for any numerical method that considers multiphase flow modeling. It enables verification of the interaction between several elements of the model, such as the balance between the pressure and interfacial forces in a complex unsteady process. In particular, this test case allows the model with a concave interface to be tested. The concave interface seems to be more difficult to resolve numerically. However, it is known that the basic RK model is able to simulate the capillary wave when the density ratio is unity [2], but to the best of the knowledge of the authors, this has not yet been done in the presence of a density ratio between the phases for an RK model. For this research, as in [51], the goal of this numerical experiment is to validate the analytical power law that relates the frequency of the capillary wave oscillation to the wave number.

Table 10. Additional simulation parameters for the two-phase capillary wave.

Case	Type	ρ_r^0/ρ_b^0
(3.5 a)	D1−V1	1
(3.5 b)	D20−V1	20
(3.5 c)	D100−V1	100
(3.5 d)	D200−V1	200
(3.5 e)	D300−V1	300
(3.5 f)	D400−V1	400
(3.5 g)	D500−V1	500

As has been done previously, we begin by describing the setting of the test. A lattice of $N_x \times N_y$ sites is used and placed over the computational domain $[1, N_x] \times [1, N_y]$. Periodic boundary conditions are used at the four ends, the fluids are initialized using the zero velocity equilibrium distribution functions, and the red fluid is initialized at the sites defined by the zone Z_1:

$$Z_1 = \{(x, y) \in \mathbb{R}^2 : -5\sin(\pi(2x-1)/N_x) + (N_y+1)/2 < y\}. \tag{40}$$

The remaining lattice sites are filled with blue fluid. Table 10 shows the additional simulation parameters for the various simulation cases. As described in section (3.1), the initial condition of this problem can lead to instability. Therefore, the first 50 000 time steps are used to stabilize that condition.

If the fluid is inviscid, the theoretical oscillation frequency ω_{the} of the capillary wave can be approximated by [52]:

$$\omega_{\text{the}} = \sqrt{\frac{\sigma_{rb}k^3}{\rho_r^0 + \rho_b^0}} \tag{41}$$

where $k = 2\pi/N_x$ is the wave number. So, the oscillation frequency obeys the power law $\omega_{\text{the}} \propto k^{3/2}$. Note that, even though this LB model doesn't neglect the viscous effects, these are sufficiently small in these simulations that the damped frequency is almost equal to ω_{the}. We now extract the numerical oscillation frequency ω_{num} of the wave from the various simulations. First, the color field ψ is defined by:

$$\psi = \frac{\rho_r - \rho_b}{\rho_r + \rho_b}. \tag{42}$$

To avoid some initial noise in the data, after $t = 5000$, at each time step, a cubic spline is constructed from ψ at the lattice sites $x = N_x/4$ and $N_y/4 < y - 1/2 < 3N_y/4$. The zero of this spline function follows the crest of the capillary wave as a function of time. Another spline function $y_{\psi=0}(t)$ is then constructed from the different crest positions. From the spline $y_{\psi=0}(t)$, we can extract the time, denoted by $t^{(1)}$, $t^{(2)}$, $t^{(3)}$, and $t^{(4)}$, at which the different subsequent local maxima and minima occur. The simulations are stopped at $t = t^{(4)}$. The numerical frequency of the capillary wave is then approximated by the following expression:

$$\omega_{\text{num}} = \frac{2\pi}{2(t^{(4)} - t^{(3)})}. \tag{43}$$

Figure 2 shows the different contours $\psi = 0$ at times $t^{(1)}$ to $t^{(4)}$ for a type D500−V1 capillary wave simulation with $N_x = 128$. We can see that the contour oscillates and is damped, as expected.

Table 11 shows the results for different capillary wave simulations using the parameters given in table 10. For different density ratios and wave numbers, a best fit line is passed through the data of $\log(\omega_{\text{num}})$ as a function of $\log(k)$. The slope of this best fit line is e_{num}, and this

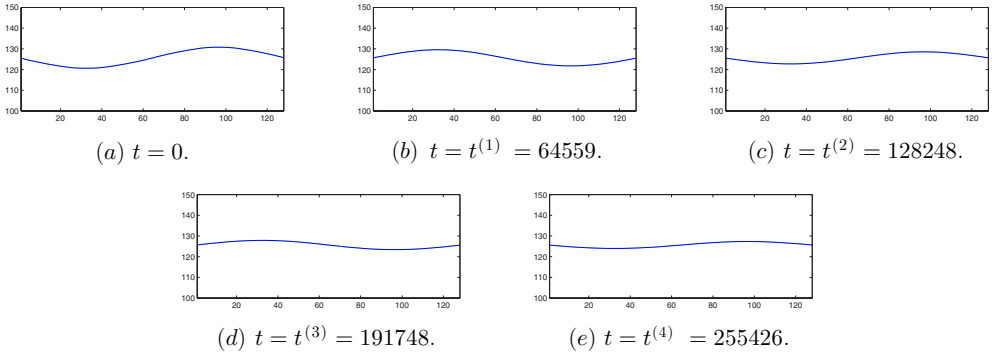

$(a)\ t = 0.$ $(b)\ t = t^{(1)} = 64559.$ $(c)\ t = t^{(2)} = 128248.$

$(d)\ t = t^{(3)} = 191748.$ $(e)\ t = t^{(4)} = 255426.$

Figure 2. Case (3.5 g): the contour of the capillary wave in an unsteady simulation.

Table 11. Linear best fit exponent e_{num} relating the numerical frequency ω_{num} and the wave number k in the theoretical expression $\log(\omega_{\text{num}}) \propto e_{\text{num}} \log(k)$ for different capillary wave simulations. Note that *r-square* is the statistical coefficient of determination.

		Wave number: k							
		1.96E-01	9.82E-02	6.54E-02	4.91E-02				
Case	Type	Frequency: ω_{num}				*r-square*	e_{num}	e_{the}	Error (%) $= 100\left\lvert\frac{e_{\text{num}} - e_{\text{the}}}{e_{\text{the}}}\right\rvert$
(3.5 a)	D1−V1	5.47E-03	2.00E-03	1.13E-03	7.43E-04	0.999 964	1.44	1.50	4.12
(3.5 b)	D20−V1	1.86E-03	6.66E-04	3.62E-04	2.37E-04	0.999 986	1.49	1.50	0.88
(3.5 c)	D100−V1	9.11E-04	3.12E-04	1.71E-04	1.11E-04	0.999 916	1.52	1.50	1.31
(3.5 d)	D200−V1	6.07E-04	2.23E-04	1.21E-04	7.86E-05	0.999 849	1.47	1.50	1.71
(3.5 e)	D300−V1	4.85E-04	1.83E-04	9.86E-05	6.39E-05	0.999 557	1.46	1.50	2.53
(3.5 f)	D400−V1	4.12E-04	1.58E-04	8.56E-05	5.51E-05	0.999 385	1.45	1.50	3.46
(3.5 g)	D500−V1	3.61E-04	1.40E-04	7.67E-05	4.93E-05	0.999 189	1.43	1.50	4.56

value should be equal to the theoretical oscillation frequency power law exponent $e_{\text{the}} = 1.5$. For each case, (3.5 a−g), the relative percentage error between the power law exponents is less than 5%.

Note that, in table 12, *r-square* is the statistical coefficient of determination. For example, an *r-square* of 0.99 means that 99% of the variance in the data is explained with the best fit line. In all our cases, the *r-square* value is more than 0.999. So, in practice, we have no difficulty in asserting that the best fit line passes almost exactly over the data points.

Overall, the results are good, and this indicates that the model is able to correctly simulate the capillary wave with variable density ratios.

3.6. Unsteady flow: two-phase oscillating cylindrical bubble

This numerical test, consisting of an unsteady oscillating cylindrical bubble, is provided as a complement to the capillary wave test case. In a previous work [14], the current model has been tested in such a flow configuration, albeit with the SRT formulation. In that study, the goal was to compare the numerical frequency of the bubble with that of the analytical frequency as a function of the surface tension. Good results were obtained with the SRT formulation,

Table 12. Additional simulation parameters for the two-phase oscillating cylindrical bubble.

Case	Type	ρ_r^0/ρ_b^0
(3.6 a)	D1−V1	1
(3.6 b)	D20−V1	20
(3.6 c)	D100−V1	100
(3.6 d)	D500−V1	500
(3.6 e)	D1000−V1	1000

and the model was stable up to a density ratio of $O(100)$. Here, the goal is similar to that with the capillary wave simulation, but in this case it is to validate the analytical power law that relates the frequency of the oscillation of the bubble as a function of its radius. Also, we are performing our tests with the MRT formulation. We will show that the maximal stable density ratio can be increased significantly with the MRT formulation compared to the SRT formulation.

A lattice size of N_x and N_y sites is used, and placed over the computational domain $[1, N_x] \times [1, N_y]$ with periodic boundary conditions at the four ends. The red and blue fluids are initialized with zero velocity equilibrium distribution functions. The sites corresponding to the red fluid are within the following initial ellipse in the zone Z_1:

$$Z_1 = \left\{ (x, y) \in \mathbb{R}^2 : \frac{(x - (N_x - 1)/2 - 1)^2}{(N_x/8)^2} + \frac{(y - (N_y - 1)/2 - 1)^2}{(3N_y/16)^2} < 1 \right\}. \tag{44}$$

The blue fluid occupies the other sites. Table 12 shows the additional simulation parameters for the various simulation cases. As explained in section (3.1), the initial condition may lead to instability, and so again, the first 2000 time steps serve only to stabilize the initial density distribution and fluid densities to a more continuous function.

As described in [53], theoretically, if the fluid is inviscid and two-dimensional, the angular frequency ω_n for each mode of the oscillations is:

$$\omega_n^2 = \frac{n(n+1)(n-1)}{\rho_r^0 + \rho_b^0} \frac{\sigma_{rb}}{R^3}. \tag{45}$$

Note that n is the mode number and R is the equivalent radius of the bubble at equilibrium. As stated in [53], we are only interested in the second mode ($n = 2$), because it corresponds to an ellipsoidal initial shape, as in our LB setting. In our specific context, we note that $\omega_{\text{the}} \equiv \omega_{n=2}$. It is important to realize that, even though the LB scheme doesn't neglect the viscous effects, once again these effects are sufficiently small in our numerical experiment that the oscillation frequency should still obey the power law $\omega_{\text{the}} \propto R^{-3/2}$.

To extract the numerical oscillation frequency ω_{num} from the simulations, we proceed as in the capillary wave test case, i.e. with equation (43). However, the cubic spline, obtained from the color field ψ, is constructed from the lattice sites $x = \lfloor (N_x - 1)/2 + 1 \rfloor$ and $(N_y - 1)/2 + 1 < y < N_y$. Also, the shape of the bubble at a given time is given by the contour $\psi = 0$. The radius R at a given time t is approximated with $R = \sqrt{(A_{\psi=0}/\pi)}$, where $A_{\psi=0}$ is the area enclosed by the contour $\psi = 0$ at time t. Figure 3 shows the different contours $\psi = 0$ at times $t^{(1)}$ to $t^{(4)}$ for the type D1000−V1 oscillating bubble simulation with $N_x = 192$. As expected, the contour of the bubble oscillates and the deformation amplitude is damped as time passes.

Table 13 shows the results of the various simulation cases. The theoretical expression $\log(\omega_{\text{num}}) \propto e_{\text{num}} \log(R)$ is well validated. The value for the radius R is the one computed at $t = t^{(4)}$. Good results are obtained as the relative errors between e_{num} and e_{the} are about 5% or

Table 13. Linear best fit exponent e_{num} relating the numerical frequency ω_{num} and the bubble radius R in the theoretical expression $\log(\omega_{\text{num}}) \propto e_{\text{num}} \log(R)$ for different oscillating bubble simulations. Note that *r-square* is the statistical coefficient of determination.

Case	Type	Variables	$N_x = 96$	$N_x = 128$	$N_x = 160$	$N_x = 192$	*r-square*	e_{num}	e_{the}	Error (%) $= 100 \left\lvert \frac{e_{\text{num}} - e_{\text{the}}}{e_{\text{the}}} \right\rvert$
(3.6 a)	D1−V1	ω_{num}	2.46E-04	1.64E-04	1.19E-04	8.91E-05	0.999 987	−1.43	−1.50	4.74
		R	14.7	19.6	24.5	29.9				
(3.6 b)	D20−V1	ω_{num}	3.75E-04	2.51E-04	1.82E-04	1.36E-04	0.999 998	−1.53	−1.50	2.27
		R	16.3	21.1	26.1	31.5				
(3.6 c)	D100−V1	ω_{num}	3.88E-04	2.60E-04	1.88E-04	1.45E-04	0.999 976	−1.58	−1.50	5.01
		R	17.0	21.8	26.8	31.7				
(3.6 d)	D500−V1	ω_{num}	1.57E-04	1.08E-04	7.96E-05	6.17E-05	0.999 962	−1.53	−1.50	2.17
		R	17.6	22.4	27.4	32.3				
(3.6 e)	D1000−V1	ω_{num}	1.01E-04	7.19E-05	5.37E-05	4.19E-05	0.999 782	−1.47	−1.50	2.14
		R	17.8	22.7	27.6	32.5				

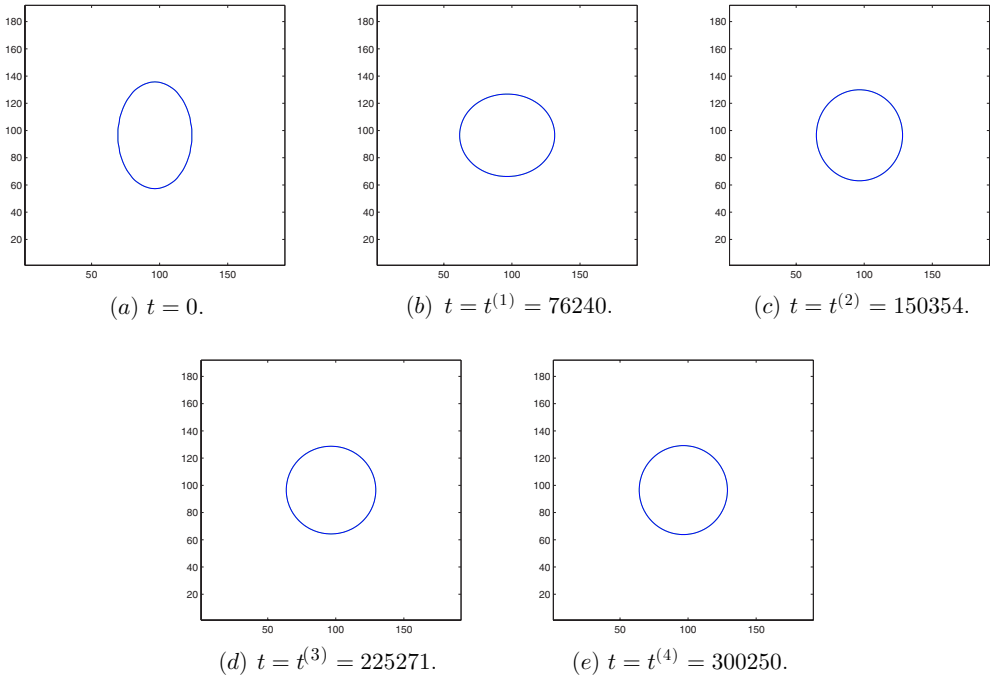

(a) $t = 0.$ (b) $t = t^{(1)} = 76240.$ (c) $t = t^{(2)} = 150354.$

(d) $t = t^{(3)} = 225271.$ (e) $t = t^{(4)} = 300250.$

Figure 3. Case (3.6 e): bubble contour in an unsteady simulation.

less up to type D1000−V1. The *r-square* value is also always greater than 0.999. Overall, it is possible to say that this theoretical power law is embedded in this LB model.

4. Conclusion

This research has enabled us to further validate the proposed lattice Boltzmann (LB) model with high density and viscosity ratios in the unsteady regime. The multiple-relaxation-time (MRT) collision operator has substantially increased the stability of the model compared to the single-relaxation-time (SRT) operator. In fact, this model has been shown to recover several complex analytical solutions to multiphase flow modeling. Owing to its simplicity, the MRT operator could be easily incorporated into other multiphase LB models available in the scientific literature. The authors believe that the MRT formulation is a step forward, and one which will enable the multiphase LB method to be applied in complex engineering applications in the near future.

Acknowledgment

The order in which the authors of this paper are listed follows the sequence-determines-credit (SDC) approach [54]. This work was supported by a grant from the NSERC (Natural Sciences and Engineering Research Council of Canada).

References

[1] Rothman D H and Keller J M 1988 Immiscible cellular-automaton fluids *J. Stat. Phys.* **52** 1119–27
[2] Gunstensen A K, Rothman D H, Zaleski S and Zanetti G 1991 Lattice Boltzmann model of immiscible fluids *Phys. Rev.* A **43** 4320–7

[3] Shan X and Chen H 1993 Lattice Boltzmann model for simulating flows with multiple phases and components *Phys. Rev.* E **47** 1815–20
[4] Swift M R, Orlandini E, Osborn W R and Yeomans J M 1996 Lattice Boltzmann simulations of liquid–gas and binary fluid systems *Phys. Rev.* E **54** 5041–52
[5] Xiaoyi H, Shan X and Doolen G D 1998 Discrete Boltzmann equation model for nonideal gases *Phys. Rev.* E **57** R13–6
[6] Santos L O E, Facin P C and Philippi P C 2003 Lattice-Boltzmann model based on field mediators for immiscible fluids *Phys. Rev.* E **68** 056302
[7] Grunau D, Chen S and Eggert K 1993 A lattice Boltzmann model for multiphase fluid flows *Phys. Fluids* A **5** 2557–62
[8] Reis T and Phillips T N 2007 Lattice Boltzmann model for simulating immiscible two-phase flows *J. Phys. A: Math. Theor.* **40** 4033–53
[9] Liu H, Valocchi A J and Kang Q 2012 Three-dimensional lattice Boltzmann model for immiscible two-phase flow simulations *Phys. Rev.* E **85** 046309
[10] Tölke J 2002 Lattice Boltzmann simulations of binary fluid flow through porous media *Phil. Trans. R. Soc. Lond. Ser.* A **360** 535–45
[11] Latva-Kokko M and Rothman D H 2005 Diffusion properties of gradient-based lattice Boltzmann models of immiscible fluids *Phys. Rev.* E **71** 056702
[12] Leclaire S, Reggio M and Trépanier J-Y 2012 Numerical evaluation of two recoloring operators for an immiscible two-phase flow lattice Boltzmann model *Appl. Math. Modelling* **36** 2237–52
[13] Leclaire S, Reggio M and Trépanier J-Y 2011 Isotropic color gradient for simulating very high-density ratios with a two-phase flow lattice Boltzmann model *Comput. Fluids* **48** 98–112
[14] Leclaire S, Reggio M and Trépanier J-Y 2013 Progress and investigation on lattice Boltzmann modeling of multiple immiscible fluids or components with variable density and viscosity ratios *J. Comput. Phys.* **246** 318–42
[15] Halliday I, Hollis A P and Care C M 2007 Lattice Boltzmann algorithm for continuum multicomponent flow *Phys. Rev.* E **76** 026708
[16] Spencer T J, Halliday I and Care C M 2010 Lattice Boltzmann equation method for multiple immiscible continuum fluids *Phys. Rev.* E **82** 066701
[17] Li X, Zhang Y, Wang X and Ge W 2013 Gpu-based numerical simulation of multi-phase flow in porous media using multiple-relaxation-time lattice Boltzmann method *Chem. Eng. Sci.* **112** 209–19
[18] Riaud A, Wang K and Luo G 2013 A combined lattice-boltzmann method for the simulation of two-phase flows in microchannel *Chem. Eng. Sci.* **99** 238–49
[19] Rannou G 2008 Lattice-Boltzmann method and immiscible two-phase flow *Master's Thesis* Georgia Institute of Technology, USA https://smartech.gatech.edu/handle/1853/26560
[20] Aidun C K and Clausen J R 2010 Lattice-Boltzmann method for complex flows *Annu. Rev. Fluid Mech.* **42** 439–72
[21] Huang H, Huang J-J, Lu X-Y and Sukop M C 2013 On simulations of high-density ratio flows using color-gradient multiphase lattice Boltzmann models *Int. J. Mod. Phys.* C **24** 1350021
[22] Leclaire S, Pellerin N, Reggio M and Trépanier J-Y 2013 Enhanced equilibrium distribution functions for simulating immiscible multiphase flows with variable density ratios in a class of lattice Boltzmann models *Int. J. Multiph. Flow* **57** 159–68
[23] McCracken M E and Abraham J 2005 Multiple-relaxation-time lattice-Boltzmann model for multiphase flow *Phys. Rev.* E **71** 036701
[24] Kuzmin A and Mohamad A A 2010 Multirange multi-relaxation time Shan–Chen model with extended equilibrium *Comput. Math. Appl.* **59** 2260–70
[25] Fakhari A and Lee T 2013 Multiple-relaxation-time lattice Boltzmann method for immiscible fluids at high Reynolds numbers *Phys. Rev.* E **87** 023304
[26] Schmieschek S, Narváez A and Harting J 2013 Multi relaxation time lattice Boltzmann simulations of multiple component fluid flows in porous media *High Performance Computing in Science and Engineering '12* (Berlin: Springer) pp 39–49
[27] Premnath K N and Abraham J 2007 Three-dimensional multi-relaxation time (mrt) lattice-Boltzmann models for multiphase flow *J. Comput. Phys.* **224** 539–59
[28] Zhao Y and Fan L-S 2010 Multirelaxation-time interaction-potential-based lattice Boltzmann model for two-phase flow *Phys. Rev.* E **82** 046708
[29] Chai Z-H and Zhao T-S 2012 A pseudopotential-based multiple-relaxation-time lattice Boltzmann model for multicomponent/multiphase flows *Acta Mech. Sin.* **28** 983–92

[30] Holdych D J, Rovas D, Georgiadis J G and Buckius R O 1998 An improved hydrodynamics formulation for multiphase flow lattice-Boltzmann models *Int. J. Mod. Phys.* C **09** 1393–404
[31] Lallemand P and Luo L-S 2000 Theory of the lattice Boltzmann method: dispersion, dissipation, isotropy, Galilean invariance and stability *Phys. Rev.* E **61** 6546–62
[32] Leclaire S 2013 Étude d'un modèle de Boltzmann sur réseau pour la simulation assistée par ordinateur des fluides à plusieurs phases immiscibles *PhD Thesis* École Polytechnique, Canada http://publications.polymtl.ca/1155
[33] Yan B, Liu H, Sun J and Zheng R 2013 Color-gradient lattice Boltzmann model for simulating droplet motion with contact-angle hysteresis *Phys. Rev.* E **88** 043306
[34] d'Humieres D 1992 Generalized lattice Boltzmann equations *Rarefied Gas Dynamics: Theory and Simulations (Progress in Astronautics and Aeronautics* vol 159*)* (Reston, VA: American Institute of Aeronautics and Astronautics) pp 450–8
[35] Premnath K N and Banerjee S 2009 Incorporating forcing terms in cascaded lattice Boltzmann approach by method of central moments *Phys. Rev.* E **80** 036702
[36] Lafaurie B, Nardone C, Scardovelli R, Zaleski S and Zanetti G 1994 Modelling merging and fragmentation in multiphase flows with surfer *J. Comput. Phys.* **113** 134–47
[37] Amiri H A A and Hamouda A A 2013 Evaluation of level set and phase field methods in modeling two phase flow with viscosity contrast through dual-permeability porous medium *Int. J. Multiph. Flow* **52** 22–34
[38] Sbragaglia M, Benzi R, Biferale L, Succi S, Sugiyama K and Toschi F 2007 Generalized lattice Boltzmann method with multirange pseudopotential *Phys. Rev.* E **75** 026702
[39] Leclaire S, El-Hachem M, Trépanier J-Y and Reggio M 2013 High order spatial generalization of 2d and 3d isotropic discrete gradient operators with fast evaluation on GPUS *J. Sci. Comput.* doi:10.1007/s10915-013-9772-2
[40] Knutson C E and Noble R D 2009 Embedding sharp interfaces within the lattice Boltzmann method for fluids with arbitrary density ratios *Eur. Phys. J. Spec. Top.* **171** 21–9
[41] Lishchuk S V, Halliday I and Care C M 2008 Multicomponent lattice Boltzmann method for fluids with a density contrast *Phys. Rev.* E **77** 036702
[42] Sidik N A C and Takahiko T 2007 Two-phase flow simulation with lattice Boltzmann method *J. Mekanikal* **24** 68–79
[43] Zalesak S T 1979 Fully multidimensional flux-corrected transport algorithms for fluids *J. Comput. Phys.* **31** 335–62
[44] Kim H and Liou M-S 2011 Accurate adaptive level set method and sharpening technique for three dimensional deforming interfaces *Comput. Fluids* **44** 111–29
[45] Zu Y Q and He S 2013 Phase-field-based lattice Boltzmann model for incompressible binary fluid systems with density and viscosity contrasts *Phys. Rev.* E **87** 043301
[46] Lätt J 2007 Hydrodynamic limit of lattice Boltzmann equations *PhD Thesis* Université de Genève, Switzerland http://archive-ouverte.unige.ch/unige:464
[47] Mateescu D, Päidoussis M P and Sim W G 1994 A spectral collocation method for confined unsteady flows with oscillating boundaries *J. Fluids Struct.* **8** 157–81
[48] Sim W-G 2006 Stratified steady and unsteady two-phase flows between two parallel plates *J. Mech. Sci. Technol.* **20** 125–32
[49] Zou Q and He X 1997 On pressure and velocity boundary conditions for the lattice Boltzmann bgk model *Phys. Fluids* **9** 1591–8
[50] Banks J W, Aslam T and Rider W J 2008 On sub-linear convergence for linearly degenerate waves in capturing schemes *J. Comput. Phys.* **227** 6985–7002
[51] Li S-M 2007 Mean-field free-energy lattice Boltzmann method For liquid-vapor interfacial flows *PhD Thesis* Virginia Polytechnic Institute and State University http://scholar.lib.vt.edu/theses/available/etd-11162007-181247
[52] Zheng H W, Shu C and Chew Y T 2006 A lattice Boltzmann model for multiphase flows with large density ratio *J. Comput. Phys.* **218** 353–71
[53] Toutant A 2006 Modélisation physique des interactions entre interfaces et turbulence *PhD Thesis* Institut National Polytechnique de Toulouse http://ethesis.inp-toulouse.fr/archive/00000503
[54] Tscharntke T, Hochberg M E, Rand T A, Resh V H and Krauss J 2007 Author sequence and credit for contributions in multiauthored publications *PLoS Biol.* **5** e18